Characterization of Microstructure, Microtexture, and Mechanical Response in UNS N08825 Superalloy/AISI 316L Stainless Steel Welds by Electron Backscatter Diffraction Analysis

Morteza Shamanian, Mahdi Babajani, Jalal Kangazian, and Jerzy A. Szpunar

The aim of this work was to characterize the microstructure-mechanical response relationships in UNS N08825/AISI 316L welds by means of electron backscatter diffraction analysis. Welding was conducted by ERNiCrMo-3 and ER308L filler wires. It was indicated that a significant increase in fractions of low Σ coincidence site lattice (CSL) boundaries occurred in UNS N08825 heat-affected zones (HAZs), whereas a small number of the boundaries formed in the AISI 316L HAZs and weld zones were of low ΣCSL types. Abnormal grain growth took place in the HAZs leading to changes in the initial texture components of the alloys. It was also demonstrated that the type of the used filler wire was a factor influencing the micro-texture components formed within the HAZs. According to the results of mechanical tests, the weldment employing the ERNiCrMo-3 filler wire exhibited superior hardness, tensile strength, and elongation. Moreover, the occurrence of the abnormal grain growth in UNS N08825 HAZs had no negative effects on the tensile response of the weldments as a result of the activation of texture strengthening mechanism. Based on the obtained results, the ERNiCrMo-3 filler metal was recommended to fabricate the joint.

1. Introduction

Minimizing the use of expensive materials is necessary in order to achieve cost savings in industrial environments. In this regard, dissimilar metal welding is a promising pathway to obtain cost savings in actual usages because it allows replacing high-expensive alloys with low-cost ones (Ref 1-3). Accordingly, dissimilar metal welding between stainless steels and Ni-based superalloy has been used in many industrial applications such as power plants, aerospace, oil and gas, and chemical industries (Ref 4-6). For instance, Safari et al. (Ref 7) reported that AISI 316 stainless steel/UNS N08825 Ni-based superalloy joints were used in aerospace industries due to their good strength and high corrosion resistance in high- and room-temperature environments.

To date, many research works have been focused on dissimilar metal welding between stainless steels and Ni-based superalloys. Ramkumar et al. (Ref 8) investigated the AISI 316L stainless steel/UNS N07718 Ni-based superalloy welds processed through continuous current gas tungsten arc welding (CCGTAW) with and without using activated flux. The results showed that no solidification cracking and/or heat-affected zone (HAZ) liquation cracking was formed in the weldments. In addition, the results of tensile tests indicated that the fracture occurred at the stainless steel parent metal, suggesting that the weld zones showed better strength than the weaker base metal. Chandrasekar et al. (Ref 9) used laser shock peening method to strengthen the AISI 316L/UNS N06625 welds developed by activated flux CCGTAW. The obtained results demonstrated that applying shock peening process resulted in the formation of compressive residual stresses in the weld zone, leading to improvement in tensile strength of the weldments. However, the weldment employing shock peening process showed slightly lower corrosion resistance than the weldment without shock peening. Safari et al. (Ref 7) investigated optical microstructure and tensile behavior of AISI 316/UNS N08825 Ni-based superalloy joints welded by CCGTAW using different filler wire types in the form of 308 stainless steel, 309 stainless steel, 316 stainless steel, and Inconel 82 Ni-based superalloy. It was observed that during all tensile testes, the AISI 316L was the weakest part of the weldment, but no detailed characterization was performed. The authors recommended welding the alloys with 309 stainless steel filler wire because the weldment employing the 309 filler wire revealed better mechanical behavior than those employing other filler wires. Ramakrishnan et al. (Ref 10) optimized the Nd:YAG pulsed laser welding of UNS N08825 and AISI 316L using Taguchi method. The authors addressed the optimum laser parameters to gain the best mechanical properties. Kulkarni et al. (Ref 11) evaluated the microstructure and mechanical properties of AISI 316L/UNS N08800 welds processed by activated flux CCGTAW. Detailed characterizations were

Morteza Shamanian and **Jalal Kangazian**, Department of Materials Engineering, Isfahan University of Technology, 8415683111 Isfahan, Iran; **Mahdi Babajani**, Advanced Materials Research Center, Department of Materials Engineering, Najafabad Branch Islamic Azad University, P.O. Box 517, Najafabad, Iran; **Jerzy A. Szpunar**, Department of Mechanical Engineering, University of Saskatchewan, Saskatoon, SK S7N 5A9, Canada. Contact e-mails: j.kangazian71@gmail.com and j.kangazian@ma.iut.ac.ir.

Table 1 Chemical composition of the base metals and filler wires (wt.%)

Element	C	Cr	Ni	Si	Mn	Ti	Mo	Nb	Cu	Al	Fe
UNS N08825	0.01	22.05	Bal.	…	0.72	0.68	3.28	…	2.18	0.12	31.28
AISI 316L	0.03	16.30	10.40	0.38	1.24	0.01	2.05	…	0.26	0.07	Bal.
ERNiCrMo-3	0.10	22.00	Bal.	< 0.50	< 0.50	…	8.00	3.61	< 0.50	< 0.40	< 0.50
ER308L	0.01	20.01	10.04	0.40	1.60	…	0.10	…	…	…	Bal.
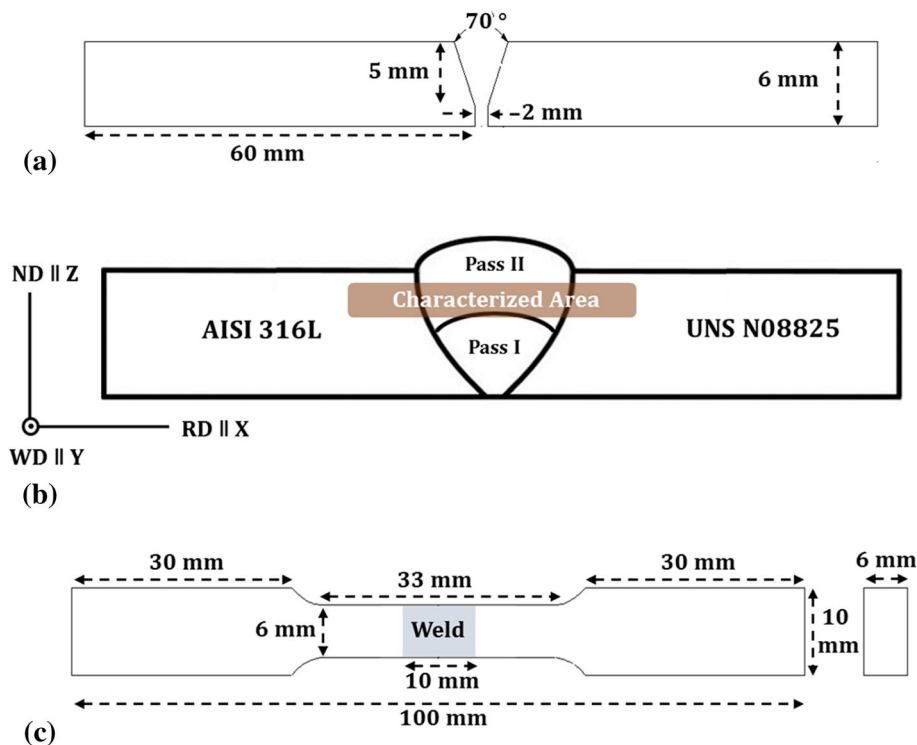
Fig. 1 Schematic of (a) joint design, (b) external framework for characterizations, and (c) dimensions of tensile specimens

utilized by means of electron probe micro-analysis, digital image correlation, and transmission electron microscope. The obtained results revealed the occurrence of a significant grain coarsening in the UNS N08800 HAZ. The presence of local microstructural heterogeneity, as well as formation of microcracks within the fusion zone, led to the deterioration of the tensile properties. However, excellent impact resistance was obtained owing to the presence of austenitic microstructure.

Review of the previous works shows that there is a scarcity of information regarding the microtexture formed within the weldments processed by fusion welding methods, which could be considered a research gap in this field. To the best of our knowledge, evaluation of microtexture-tensile response of the Ni-based superalloys/stainless steels welds has not been reported in the available literature works. Thus, the motivation of this work is to characterize the Ni-based superalloys/stainless steels dissimilar welds in terms of microtexture evolution and microstructure-mechanical response correlation by means of electron backscatter diffraction (EBSD) analysis. We previously studied the effect of current types (i.e., continuous current and pulsed current) on the microstructure, microtexture, and corrosion behavior of UNS S32750 stainless steel/UNS N08825 Ni-based superalloy welds (Ref 12). The aim of the current work is to investigate detailed characterizations of AISI

316L/UNS N08825 weldments produced by ER308L and ERNiCrMo-3 filler wires. Microstructure, microtexture, hardness, and tensile behavior of the weldments are evaluated, too.

2. Experimental Procedure

2.1 As-Received Materials and Welding

The as-received alloys used in this study were UNS N08825 Ni-based superalloy and AISI 316L austenitic stainless steel plates with dimensions of $300 \times 60 \times 6$ mm. Chemical compositions of the materials are presented in Table 1. Before welding, a single-V joint design was prepared as schematically depicted in Fig. 1(a). Some acetone solution and SiC papers were used to remove any surface contamination of the base metals and filler wires. Two types of filler wires in the form of ERNiCrMo-3 Ni-based superalloy and ER308L stainless steel combined with CCGTAW process were employed to weld the as-received alloys. The used welding parameters are listed in Table 2. During welding, a W-2%ThO$_2$ non-consumable electrode with 2.4 mm diameter, purging and shielding gases (99.99% pure Ar) with the flow rates of 9-15 L/min were used.

Table 2 The specifications of the samples

Sample	Pass	Filler wire	Current, A	Voltage, V	Travel speed, mm/s	Heat input, kJ/mm
No. 1	1	ERNiCrMo-3	170	12	1.2	1.15
	2	ERNiCrMo-3	150	11	1.3	0.87
No. 2	1	ER308L	170	12	1.3	1.06
	2	ER308L	150	11	1.4	0.82
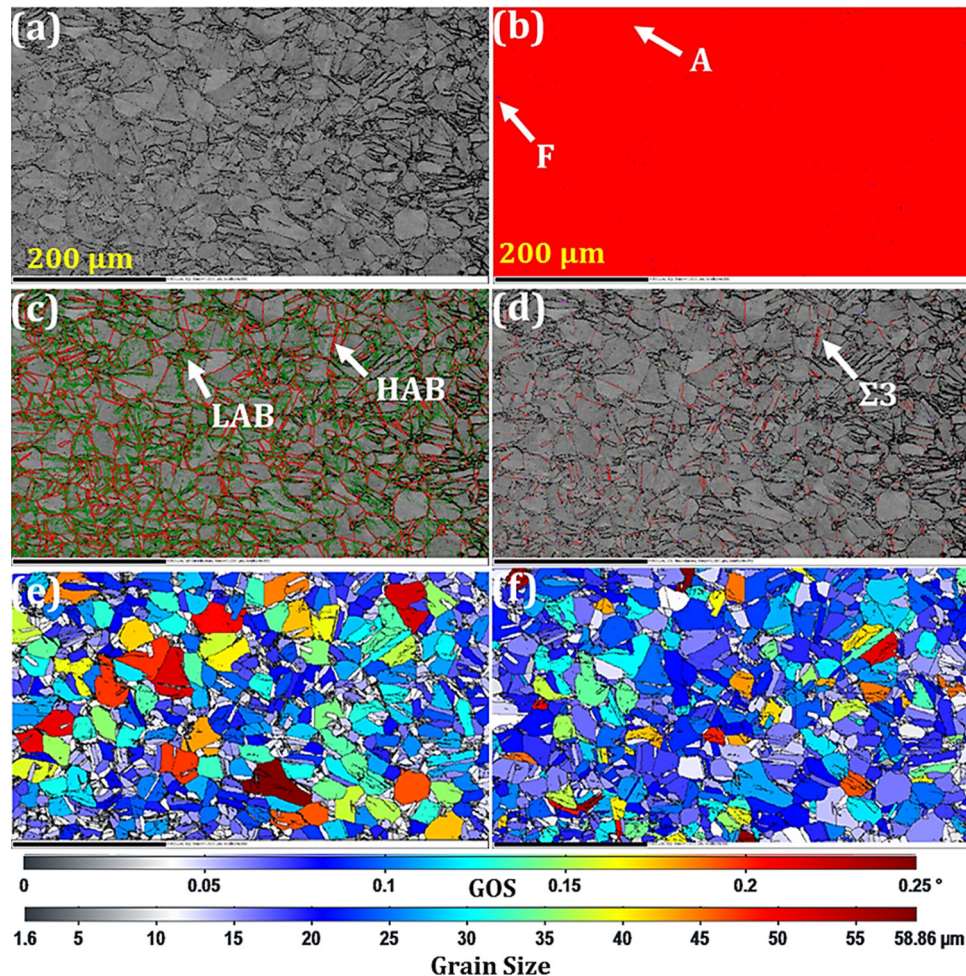
Fig. 2 EBSD maps of the AISI 316L base metal: (a) image quality, (b) phase map (A: Austenite, F: Ferrite), (c) boundaries distribution map (Red: HAB, Green: LAB), (d) CSL boundaries distribution map (Red: Σ3), (e) grain size map, and (f) GOS map

2.2 Characterization

After welding, wire-cut discharge machining was used to extract a series of samples from the weldments, and the extracted samples were subjected to typical metallography processes. After grounding by SiC papers (up to #2400), some diamond-bearing pastes were used to polish the samples, which were then polished with some basic colloidal Silica slurry (50 nm). After drying, the prepared samples were loaded in a field emission scanning electron microscope (Hitachi SU8230) chamber equipped with an EBSD detector. The area subjected to characterization processes is schematically depicted in Fig. 1(b). The EBSD analysis was performed with a step size of 1-2 μm. The data visualization and post-processing were conducted by using the HKL CHANNEL5 and ATEX software (Ref 13). The framework used for the EBSD analysis is also shown in Fig. 1(b), where ND, WD, and RD are related to the normal direction, welding direction, and rolling direction, respectively.

2.3 Mechanical Tests

Two types of mechanical tests were performed to evaluate room-temperature mechanical behavior of the weldments. The variation in microhardness values at the cross section view was examined using a microhardness tester equipped with a Vickers pyramid indenter. Upon microhardness tests, a 0.3 kg (300 g) load with a 10 s dwell time was applied.
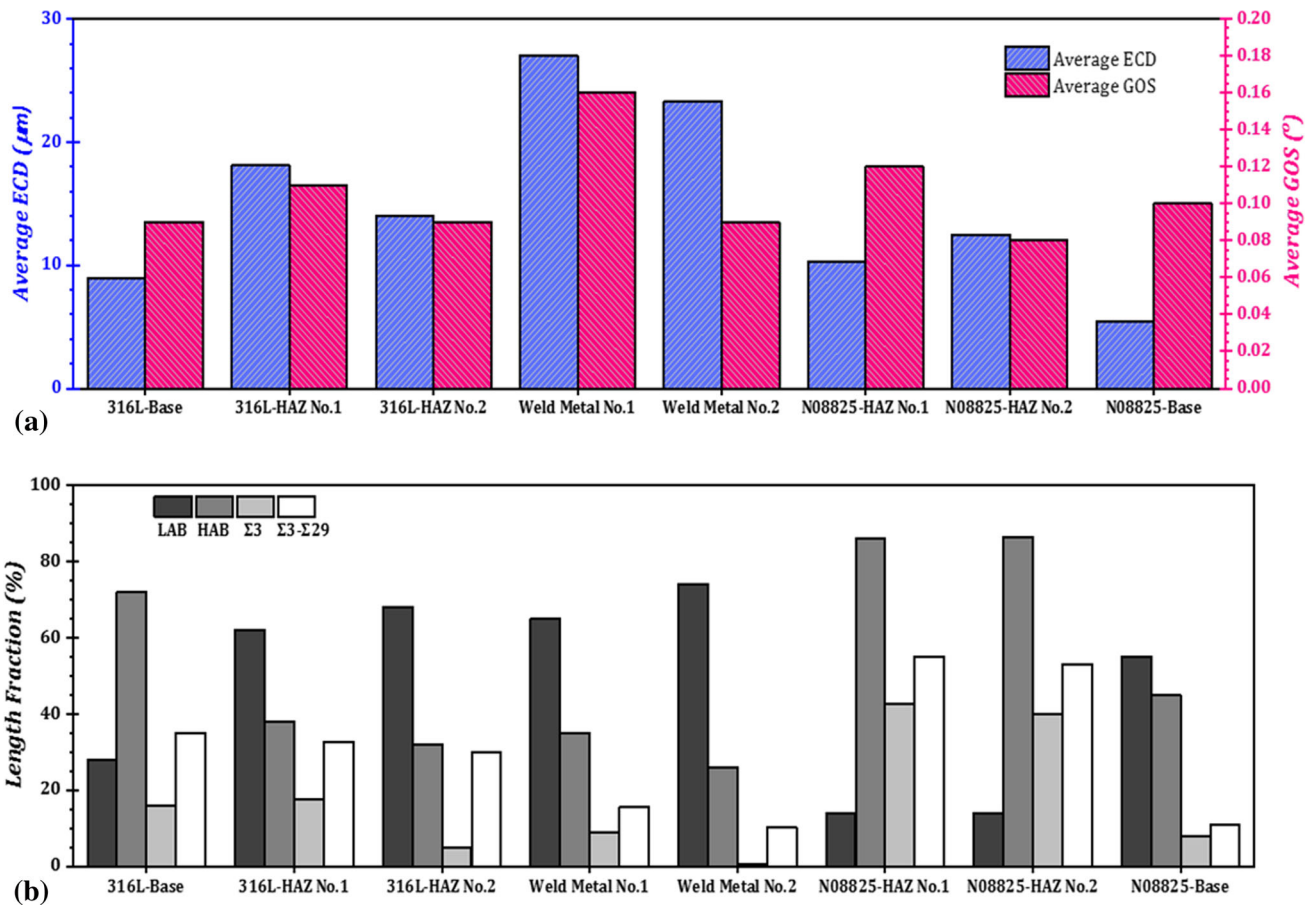
Fig. 3 The quantitative measurements of (a) grain size and average GOS, and (b) boundaries characters across the weldments for the austenite phases

According to the ASTM E8, sub-sized transverse tensile specimens (100 × 10 × 6 mm) with a dog-bone shape having the dimensions shown in Fig. 1(c) were extracted from the weldment by means of wire-cut discharge machining. The extracted specimens were subjected to tensile tests with a crosshead speed of 2 mm/min at room temperature. After performing the tensile tests, the fracture surfaces were examined by SEM. Both microhardness and tensile tests were repeated at least three times, and the average values were reported.

3. Results and Discussions

3.1 Microstructure

Figure 2 displays the microstructure of the AISI 316L stainless steel base metal. The phase map (Fig. 2b) reveals that the 316L base metal consisted of austenitic matrix with a small amount (up to 0.3%) of ferrite phase. Formation of the ferrite phase within the austenitic matrix of the austenitic stainless steels was due to the segregation of the ferrite-promoting elements like Cr (Ref 14). Average grain size of the austenite phase in the weldments was evaluated in terms of the equal circle diameter (ECD) as shown in Fig. 3(a). The average ECD of austenite phase in the 316 L base metal was found to be 8.9 μm. The boundaries within the 316 L base metal were divided

into two groups in the form of high-angle boundaries (HABs) with a misorientation higher than 15°, and low-angle boundaries (LABs) with a misorientation lower than 15°, which are colored in red and green in Fig. 2(c), respectively. A detailed statistical analysis (Fig. 3b) indicated that fractions of the HABs and LABs were 72 and 28%, respectively. Figure 2(s) shows that a small amount (∼ 35%) of the HABs formed within the 316L base metal had special characters known as coincidence site lattices (CSLs). Generally, presence of low $\sum$CSL boundaries (i.e., $\sum3$-$\sum29$) in the microstructure could improve the properties of alloys, especially the inter-granular corrosion resistance (Ref 15). The degree of misorientation within grains was investigated in terms of grain orientation spread misorientation (GOS) parameter. The GOS parameter shows the average point-to-origin misorientation within a grain, suggesting the long-range misorientation (Ref 16, 17); thus, it shows the overall plastic deformation (i.e., lattice curvatures) of a grain. The results of statistical analysis regarding the average GOS are shown in Fig. 3(a). As can be seen, the average GOS of the stainless steel base metal was found to be 0.09°.

Figure 4 presents the EBSD maps of UNS N08825 base metal, which contained equiaxed austenitic phase matrix and some Ti (N, C) precipitates. The presence of Ti (N, C) precipitates within the microstructure of superalloys has also been reported in previous research works (Ref 18-20). Figure 3(a) indicates that average ECD of the austenite phase was 5.4 μm. In addition, average GOS was found to be 0.1°. Unlike the stainless steel base metal, a significant amount of LABs (∼
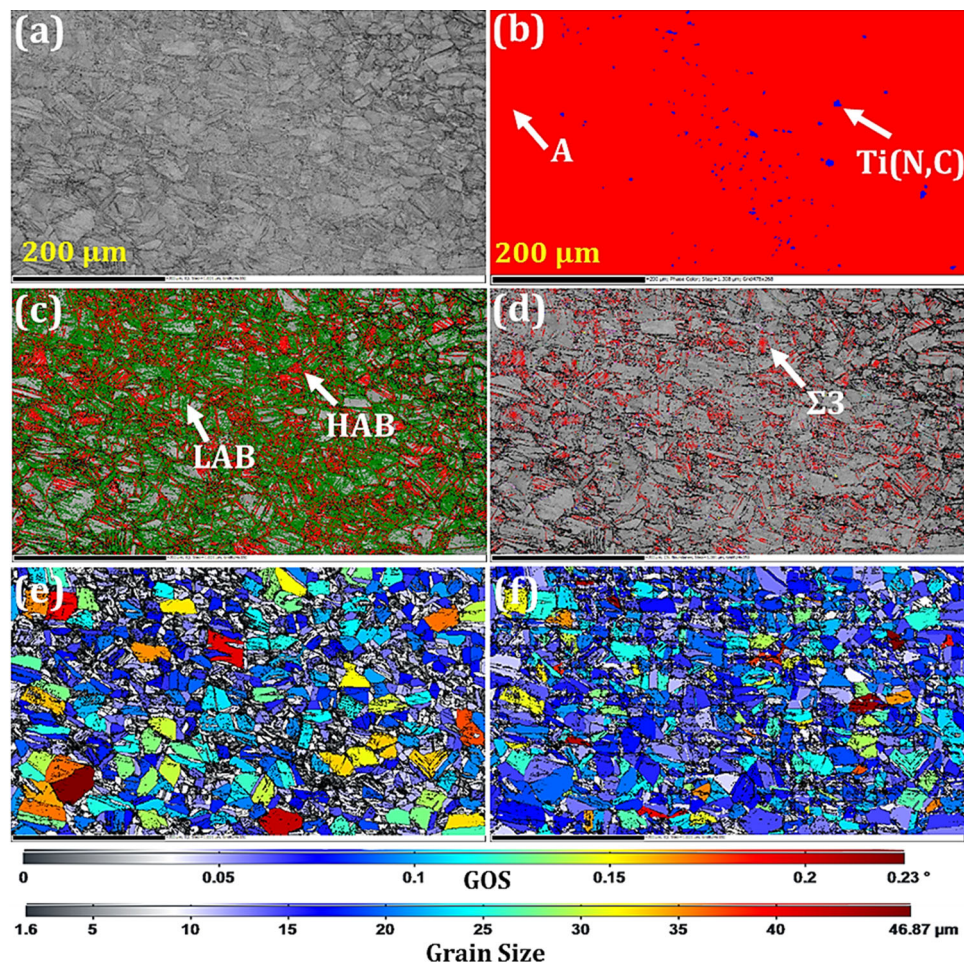
Fig. 4 EBSD maps of the UNS N08825 base metal: (a) image quality, (b) phase map (A: Austenite), (c) boundaries distribution map (Red: HAB, Green: LAB), (d) CSL boundaries distribution map (Red: $\Sigma 3$), (e) grain size map, and (f) GOS map

55%) was formed in UNS N08825 parent metal. The HABs rarely showed special character; hence, the fraction of the CSLs boundaries was found to be around 11%. The fraction of $\Sigma 3$ CSLs within UNS N08825 base metal ($\sim 8\%$) was half of that within the stainless steel base metal ($\sim 16\%$). The $\Sigma 3$ CSL is first-order CSL orientation relationship with 60° rotation around $<111>$ axis which could present the twin boundaries (Ref 21, 22). Thus, it meant that more twin-induced low $\sum$CSL grain boundaries were formed in the stainless steel base metal as compared to UNS N08825.

Figure 5 and 6 shows the EBSD maps of the AISI 316L/ weld metal interfaces for No. 1 and No. 2 samples, respectively. The phase maps reveal that the HAZs had an austenite matrix with a small amount (up to 0.2%) of ferrite phase. Average ECD of the austenite phase in 316L HAZs was found to be around 18 and 14 µm. Considering the average ECD of AISI 316L base metal, the data indicated that abnormal grain growth occurred in 316L HAZs, which was due to the thermal cycles experienced by the materials during welding passes (Ref 18). Fractions of the LABs formed within 316L HAZs were found to be 62-68%, which were higher than those formed in the intimal 316L. It meant that more fractions of dislocations were generated in the HAZs, as results of the presence of residual stresses in the HAZs (Ref 23). On the other hand, the average GOS in 316L HAZs was found to be 0.11° and 0.09° for No. 1 and No. 2 samples, respectively. As can be seen, although

residual stresses could be generated in the HAZs, the average GOS of 316L HAZs was similar to the 316L base metal. Considering the grain size in HAZs and base metals, the average ECD of 316L HAZs was higher than that of the related base metal; hence, the misorientation spreads over large grains in HAZs, as compared to the 316L base metals. Accordingly, it is inferred that the average misorientation of HAZs' grains was not significantly affected by the residual stresses raised from the welding process. The fractions of CSLs in 316L HAZs were found to be around 29.9-32.6%, which were similar to those in 316L base metal suggesting that the grain growth had no significant effect on the fractions of low ΣCSLs.

Figure 7 and 8 displays the EBSD maps of UNS N08825/ weld metal interfaces for No. 1 and No. 2 samples, respectively. Some Ti (N, C) precipitates were observed in UNS N08825 HAZs. Average ECDs of the austenite phase in UNS N08825 HAZs were found to be 10.3 and 12.5 µm for No. 1 and No. 2 samples, respectively. Similar to 316L HAZs, abnormal grain growth occurred in UNS N08825 HAZs. The results were in good agreement with the previous work (Ref 7, 18). Kulkarni et al. (Ref 11) reported that dissolution of grain boundaries' precipitates resulted in suppressing the pinning action leading to the abnormal grain growth in HAZs. Fractions of the LABs formed in UNS N08825 HAZs were found to be 14 and 13.8% for No. 1 and No. 2 samples, respectively. Considering the fraction of LABs in UNS N08825 base metal, a significant
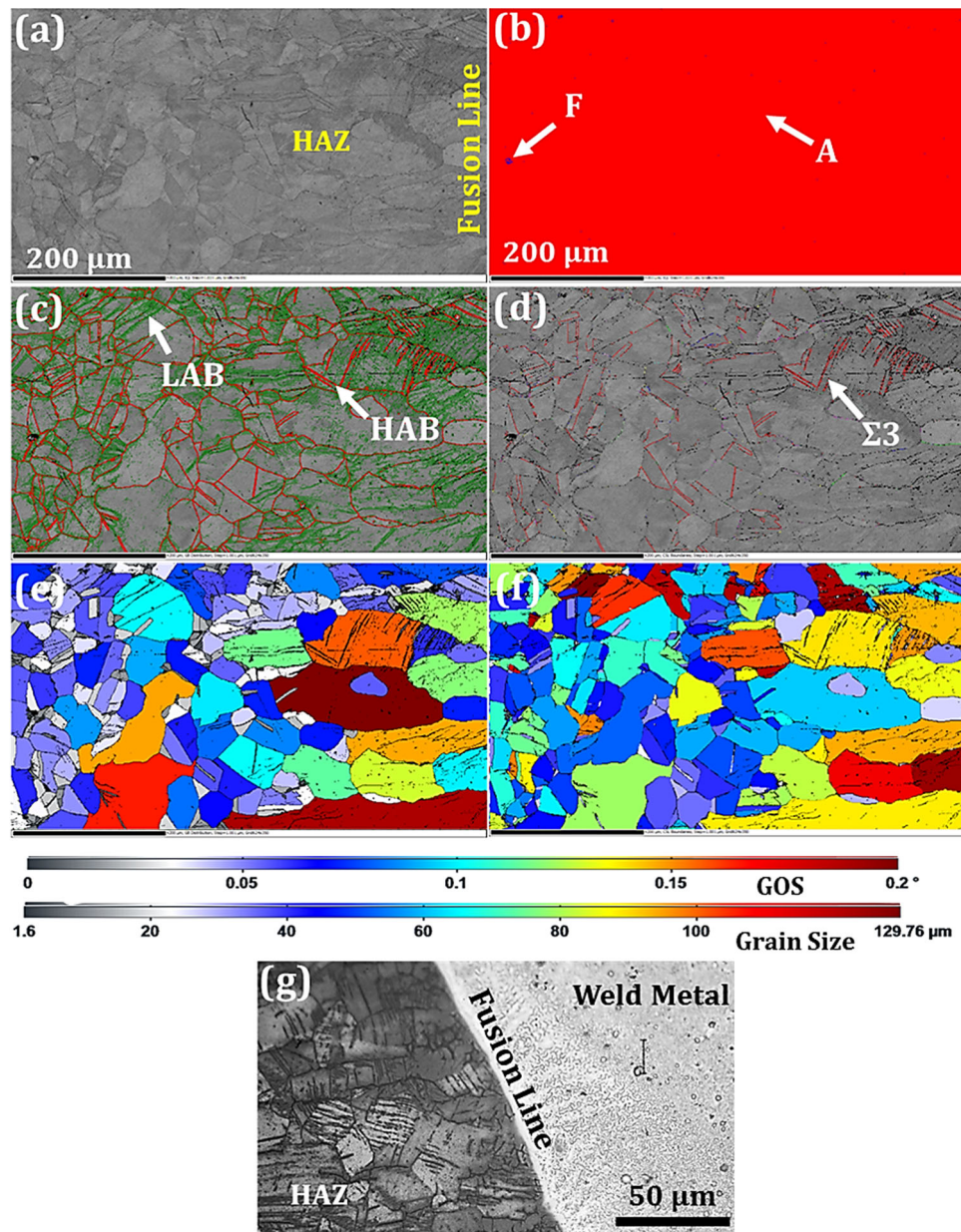
Fig. 5. EBSD maps of the AISI 316L/No. 1 weld metal interface: (a) image quality, (b) phase map (A: Austenite, F: Ferrite), (c) boundaries distribution map (Red: HAB, Green: LAB), (d) CSL boundaries (Red: Σ3), distribution map, (e) grain size map, and (f) GOS map, (g) optical microstructure of the interfaces (Color figure online)

reduction in the LABs was observed in UNS N08825 HAZs, which could be attributed to the tempering effect of the welding process on it. In other words, during welding, an increase in the temperature of the base metal adjacent to the fusion line caused the annihilation of some dislocations, leading to the occurrence of the recovery process in UNS N08825 HAZs. Regarding the misorientation of UNS N08825 HAZs' grains, the average GOS in UNS N08825 HAZs was similar to the base metals, meaning that using the welding process had no significant effect on the lattice curvature of UNS N08825's grains near the fusion line. The statistical analysis (Fig. 3b) demonstrated that the fraction of the CSL boundaries in UNS N08825 HAZs was significantly higher than that of the related base metal. It could be inferred that apart from the abnormal grain growth, applying the welding processes had no significant negative effects on the

microstructure of UNS N08825 side. Overall, it is observed that although both UNS N08825 and 316L underwent abnormal grain growth in HAZs, the misorientation and boundaries characters of UNS N08825 HAZs and 316L HAZs were different as compared to the related base metals.

Microstructures of the weld metals are presented in Fig. 6, 7, and 8. Regarding both No. 1 and No. 2 welds, the occurrence of the epitaxial growth resulted in the formation of the columnar grains adjacent to the fusion lines. Since the base metals and the filler wires had the same crystal structure, i.e., face-centered cubic (FCC) type, the epitaxial growth was dominant in the weld metal/base metal interfaces (Ref 24). Average ECDs of the columnar grains were found to be around 27 and 23 μm for No. 1 and No. 2 weld metals, respectively. Fractions of the LABs were 65% and 74% for No. 1 and No. 2 samples, respectively.
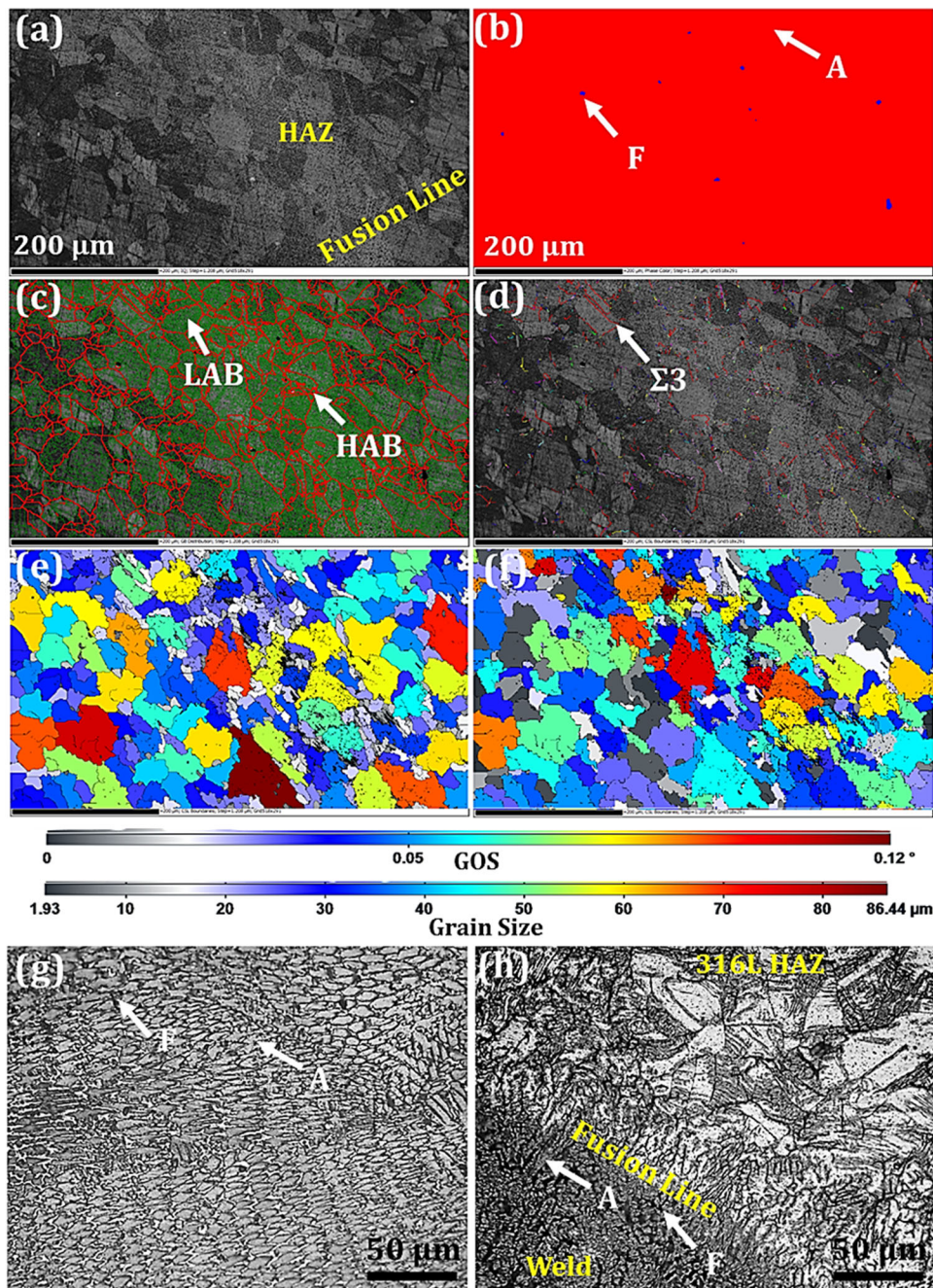
Fig. 6 EBSD maps of the AISI 316L/No. 2 weld metal interface: (a) image quality, (b) phase map (A: Austenite, F: Ferrite), (c) boundaries distribution map (Red: HAB, Green: LAB), (d) CSL boundaries distribution map (Red: Σ3), (e) grain size map, and (f) GOS map, optical microstructure of (g) the No. 2 weld centerline, and (h) AISI 316L/No. 2 weld metal interface (Color figure online)

The fractions of the LABs in the weld zones were higher than those in the base metal, as a result of the presence of residual stresses in the weld zones (Ref 23). The detailed statistical analysis also showed that a few HABs were of low ΣCSL types, which could be due to the as-cast nature of the grains formed within the weld zones. On the other hand, average GOSs in No. 1 and No. 2 weld zone were found to be 0.16° and 0.09°, respectively, which were almost similar to those of the base metals.

In the weld centerline, the morphology of grains was in the form of equiaxed type. The solidification rate (R) and maximum temperature gradient (G) are the main parameters determining the type and size of the solidification microstructure within the weld metals (Ref 24, 25). The changes in the morphology of grains from fusion line toward the centerline could be explained by the G/R ratio. From fusion line toward the centerline, the G/R ratio has a decreasing trend. Moreover, a decrease in the G/R ratio promotes the constitutional supercooling (Ref 25, 26). Therefore, the columnar grains were formed in the weld zone near the weld fusion line, while in the weld centerline, the equiaxed grains were formed. Microstructure of No. 1 weld zone consisted of austenitic matrix with a
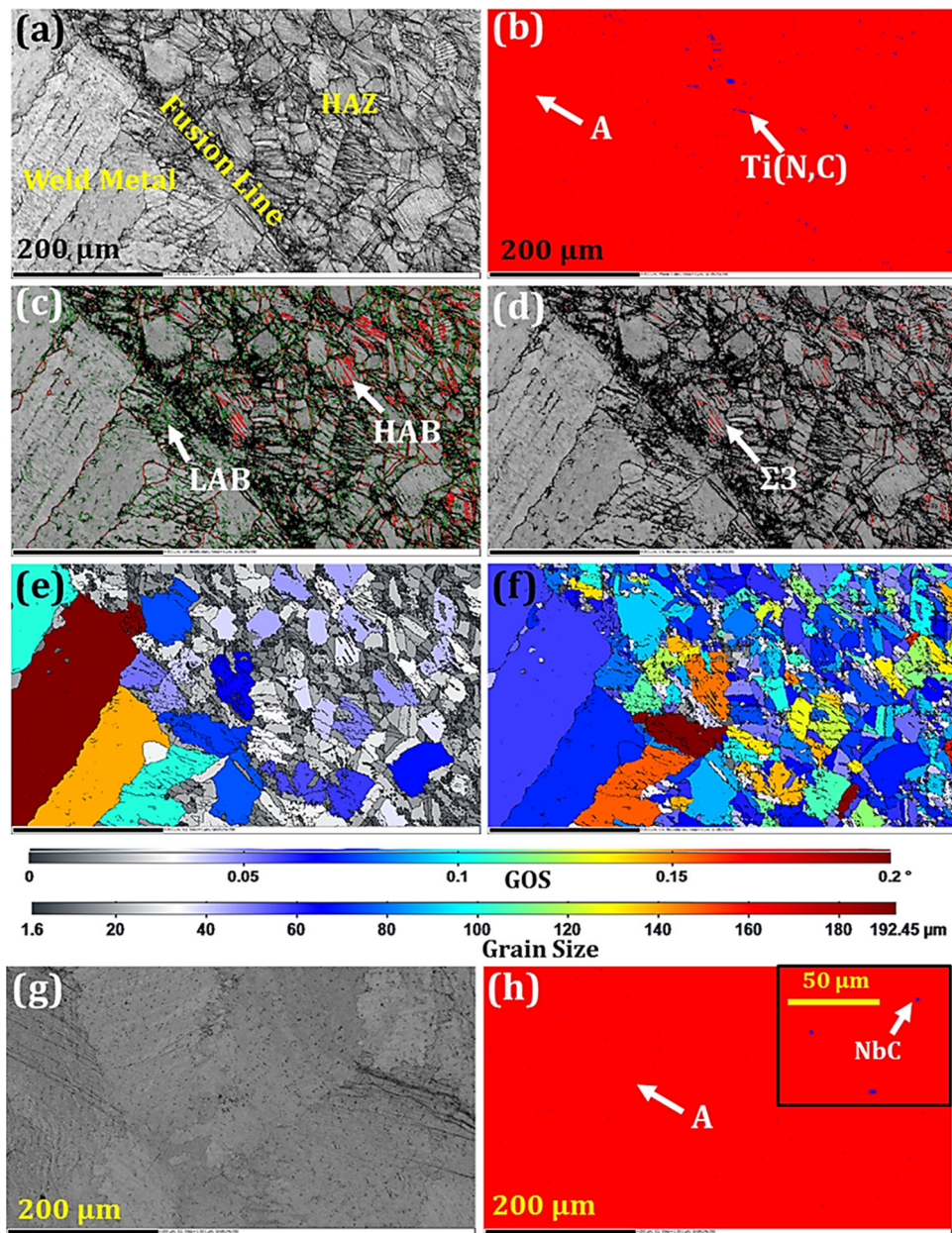
Fig. 7 EBSD maps of the UNS N08825/No. 1 weld metal interface: (a) image quality, (b) phase map (A: Austenite), (c) boundaries distribution map (Red: HAB, Green: LAB), (d) CSL boundaries distribution map (Red: Σ3), (e) grain size map, and (f) GOS map, EBSD maps of the No. 1 weld metal centerline: (g) image quality, and (h) phase map (A: Austenite) (Color figure online)

small number (∼ 0.5%) of NbC precipitates. It should be noted that the step size used in the EBSD observations was 1 μm; thus, more precipitations, i.e., submicron precipitates, could be presented in No. 1 weld zone. Formation of the NbC precipitates within the weld zone was due to the segregation of Nb element (Ref 27). The presence of Mo-rich and Nb-rich precipitates in the inter-dendritic regions of the weld metals employing the ERNiCrMo-3 filler wire was also reported in previous research works (Ref 28-30). Silva et al. (Ref 31) studied the solidification behavior of UNS N06625 Ni-based superalloy. They observed that precipitates formed in UNS N06625 upon solidification were complex carbide/nitride particles, such as NbC, (NbTi) C and TiN, and/or Lave phase. It is worth mentioning that the chemical composition of the ERNiCrMo-3 filler wire corresponded to that of UNS N06625

Ni-based superalloy. On the other hand, according to Fig. 6(g) and (h), No. 2 weld metal contained some ferrite phase (up to 7%) in the austenitic matrix. Similar observations were reported in literature works (Ref 7, 32, 33) regarding the microstructure of the weld metals employing the austenitic filler wires.

3.2 Microtexture

The microtexture evolution across the weldments was investigated in terms of the orientation distribution function (ODF). The inverse pole-figure (IPF) maps and the ODF sections of the base metals are presented in Fig. 9. Both AISI 316L and UNS N08825 base metals showed low intensities in the ODF sections suggesting the presence of weak texture components formed within the base metals. In the ODF of base
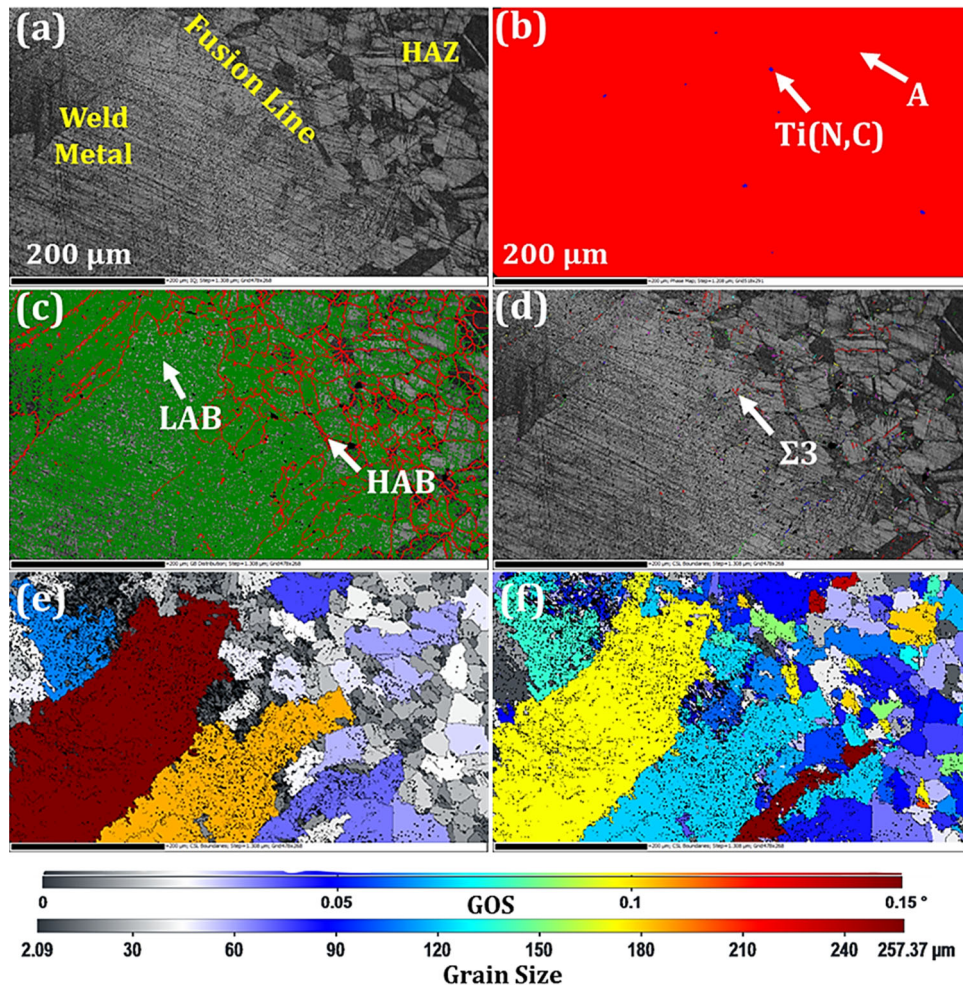
Fig. 8 EBSD maps of the UNS N08825/No. 2 weld metal interface: (a) image quality, (b) phase map (A: Austenite), (c) boundaries distribution map (Red: HAB, Green: LAB), (d) CSL boundaries distribution map (Red: Σ3), (e) grain size map, and (f) GOS map (Color figure online)

metals, the maximum intensities were observed in Bunge notations $(\phi_1, \phi, \phi_2) = (37°, 0°/90°, 0°)$, $(0°, 0°, 45°)$, $(35°, 60°, 30°)$, and $(82°, 0°$ to $40°, 45°)$. Evaluations of the components showed that the texture components observed in the ODF sections were not well-known texture components formed in FCC metals, but the presence of $(90°, 30°, 35°)$ components could be related to the well-known Brass Rex $(82°, 30°, 34°)$ texture component (Ref 34, 35).

Figure 10 reveals the IPF maps and ODF sections of HAZs of No. 1 sample. The texture components formed in the base metal completely disappeared in 316L HAZ. Two texture components having Bunge notations $(0°, 52°, 0°)$ and $(85°, 90°, 50°)$ were observed. These components could correspond to Goss $(0°, 45°, 0°)$ and Twin to Cu $(90°, 80°, 45°)$ components, respectively. Regarding UNS N08825 HAZ, the components were almost similar to those formed in the base metals although there was up to 15° shift for the Bunge notations of UNS N08825 HAZ's components in comparison with those observed in the base metals. Moreover, Bunge notation $(80°, 60°, 35°)$ was only observed in UNS N08825 HAZ.

The IPF color maps, PFs, and ODF sections of HAZs of No. 2 sample are presented in Fig. 11. According to the ODF sections of 316L HAZ, Bunge notation $(0°, 37°, 30°)$ and $(60°, 45°, 70°)$ showed maximum intensities. On the other hand,

Bunge notations $(30°, 37°, 0°)$ and $(30°, 75°, 25°)$ had maximum intensities at UNS N08825 HAZ. Based on the PFs, both UNS N08825 HAZ and 316L HAZ showed Y ∥ {111} relationship corresponding to the WD ∥ {111} fiber. In addition, the X ∥ {111} relationship corresponding to RD ∥ {111} was only formed in UNS N08825 HAZ.

Figure 12 presents the IPF maps and ODF sections of the weld metals. According to the ODF sections of weld metals adjacent to the fusion lines, Bunge notations $(75°, 20°, 45°)$ and $(60°, 45°, 60°)$ showed the maximum intensities in No. 1 and No. 2 samples, respectively. The ODF sections of No. 1 weld centerline (Fig. 12d) had maximum at Bunge notations $(30°, 20°, 10°)$, $(60°, 85°, 35°)$, and $(57°, 30°, 65°)$. As can be seen, the components formed in the fusion line were significantly different as compared to those formed in the weld centerline. It meant that no preferential orientation was formed within the weld zone, suggesting that random texture was dominant in the weld metal.

Considering the welding parameters used to produce the weldments (Table 2), as can be seen, the heat inputs (HIs) were almost the same. However, the microtexture studies demonstrated that the orientation of grains in the weldments employing ERNiCrMo-3 and ER308L was significantly different. Hence, it is inferred that the used filler wire could be
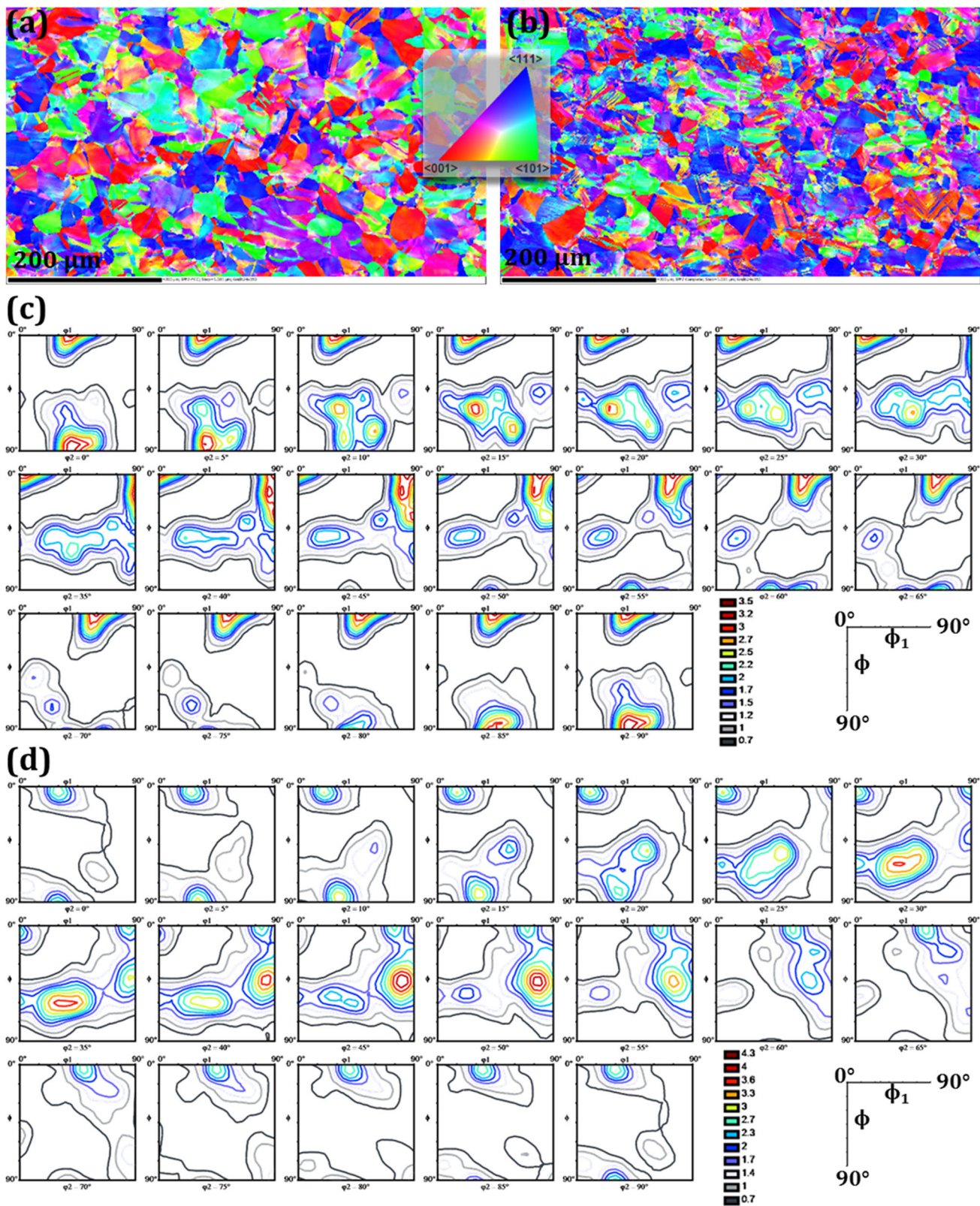
Fig. 9 The WD IPF color maps and ODF sections of austenite phase: (a, c) AISI 316L, and (b, d) UNS N08825 base metals

considered a parameter influencing the microtexture of the weldments. Because the chemical composition of the used filler wires was different (Table 1), it could be expected that thermal properties of the weld metals were also different. Therefore, the changes in the microtexture of the weldment at the same HI value could be attributed to the differences in the heat transfer from the weld metals toward the parent metals. It is well known that the orientations of grains in HAZs and weld metals are
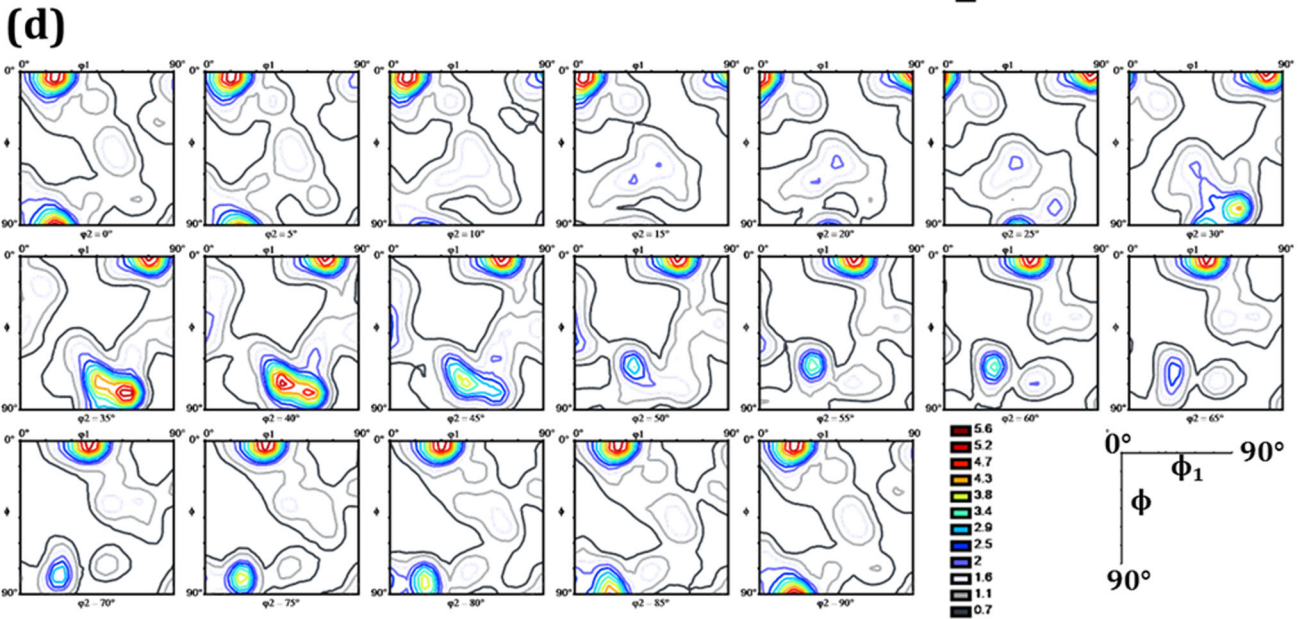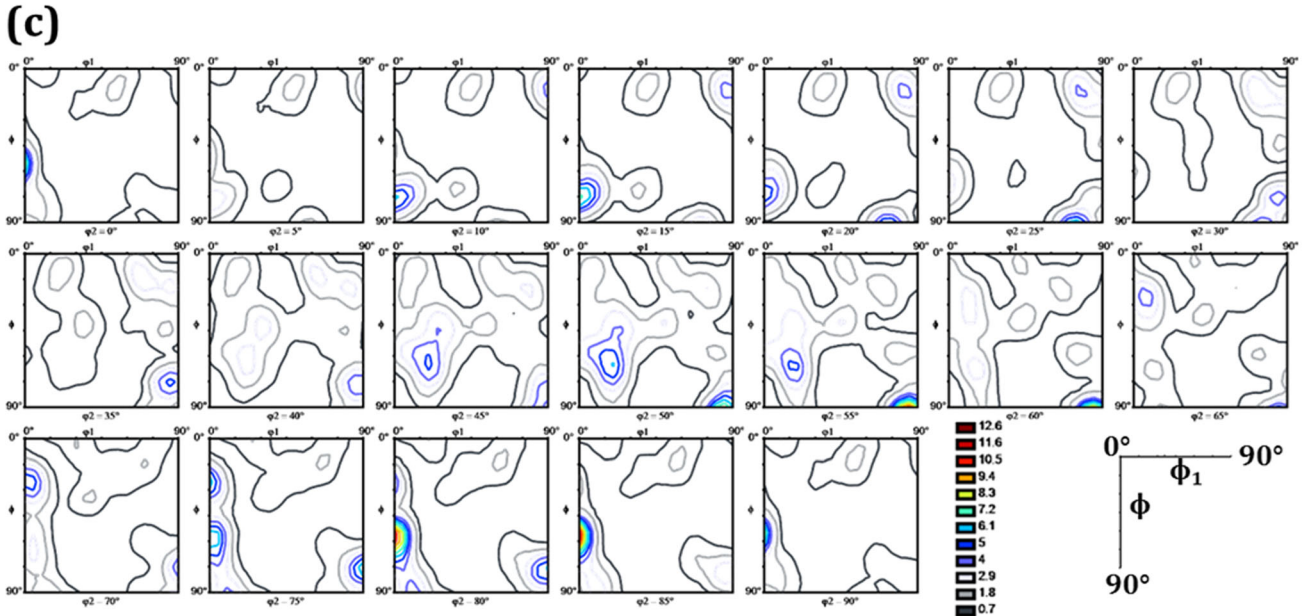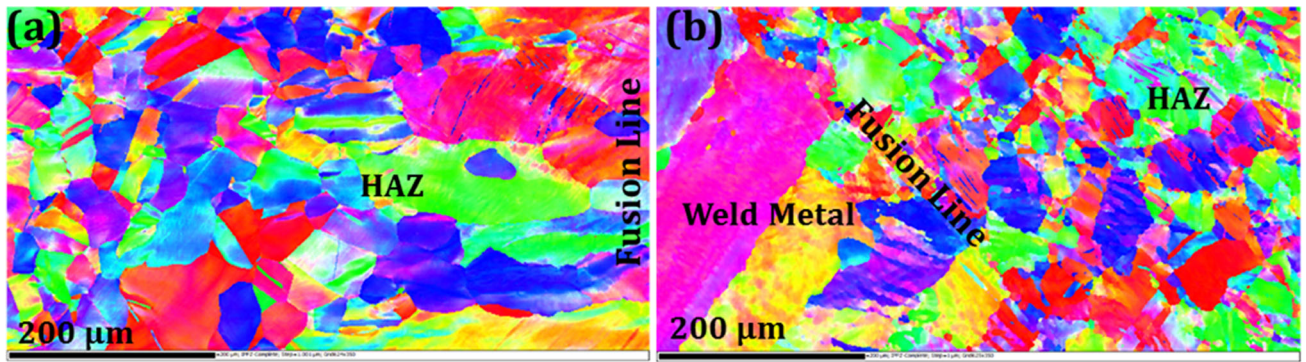
Fig. 10 The WD IPF color maps and ODF sections of No. 1 HAZs for austenite phase: (a, c) AISI 316L, and (b, d) UNS N08825 sides
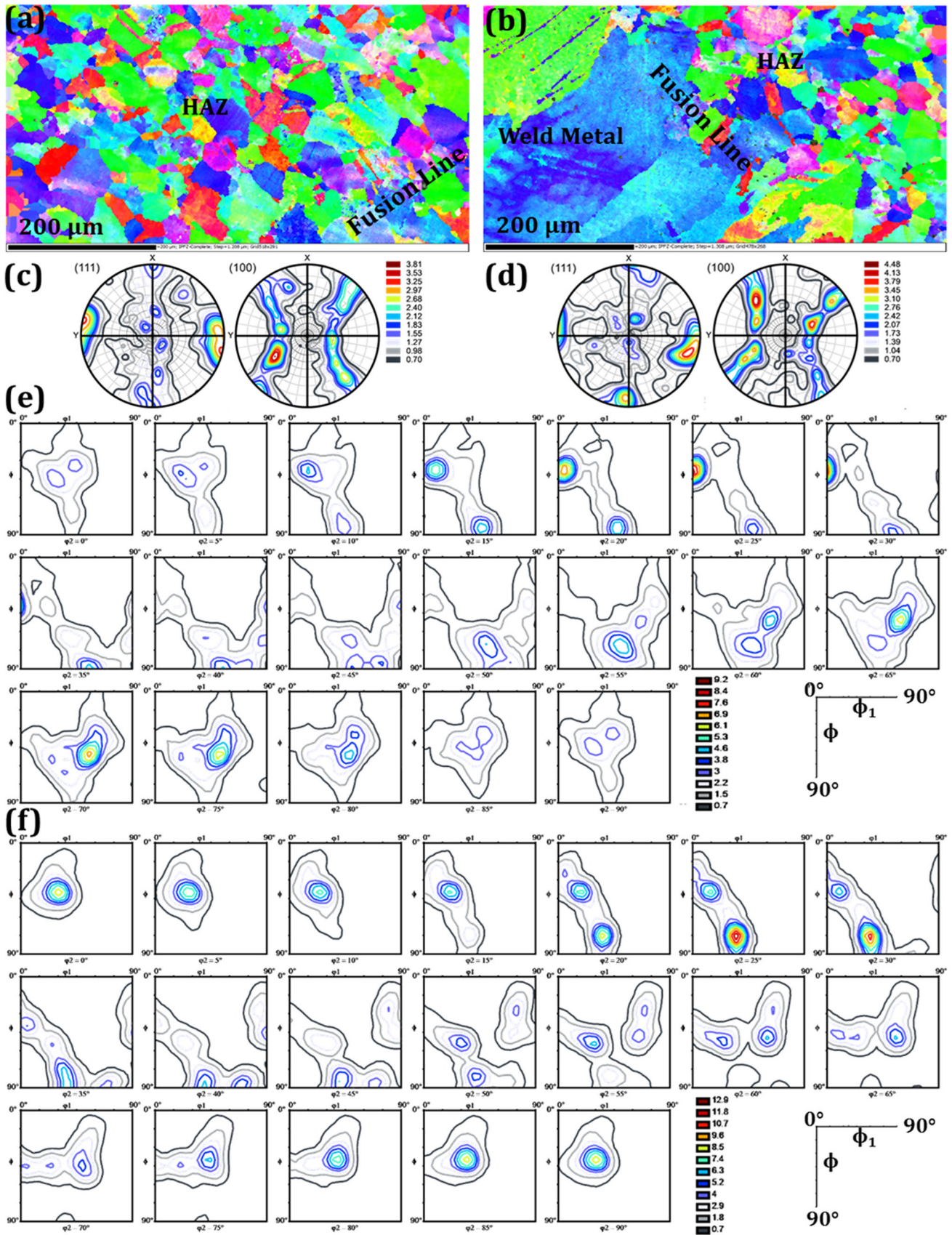
Fig. 11 The WD IPF color maps, PFs, and ODF sections of No. 2 HAZs for austenite phase: (a, c, e) AISI 316L, and (b, d, f) UNS N08825 sides (Color figure online)
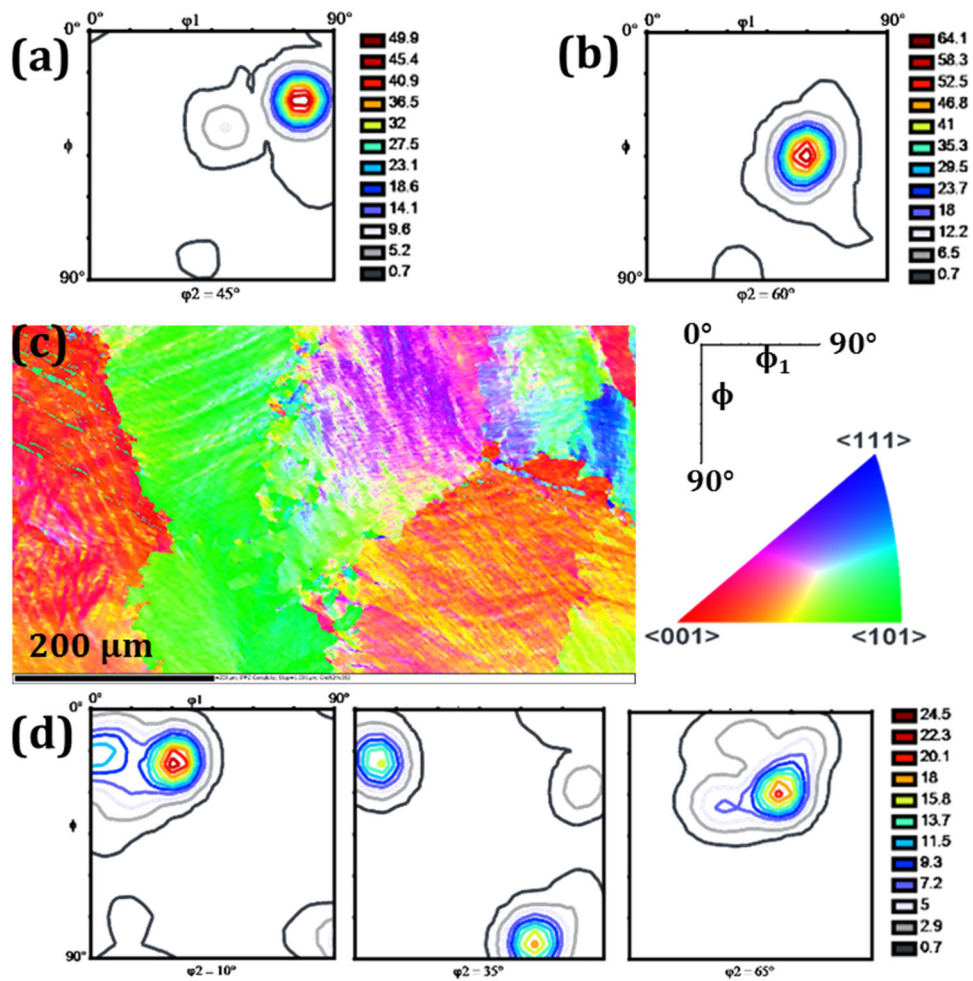
Fig. 12 (a) ODF section of the No. 1 weld near fusion line of UNS N08825 side for austenite phase, (b) ODF section of the No. 2 weld near fusion line of UNS N08825 side for austenite phase, (c) WD IPF color maps of No. 1 weld centerline for austenite phase, and (d) ODF sections of the No. 1 weld centerline for austenite phase (Color figure online)
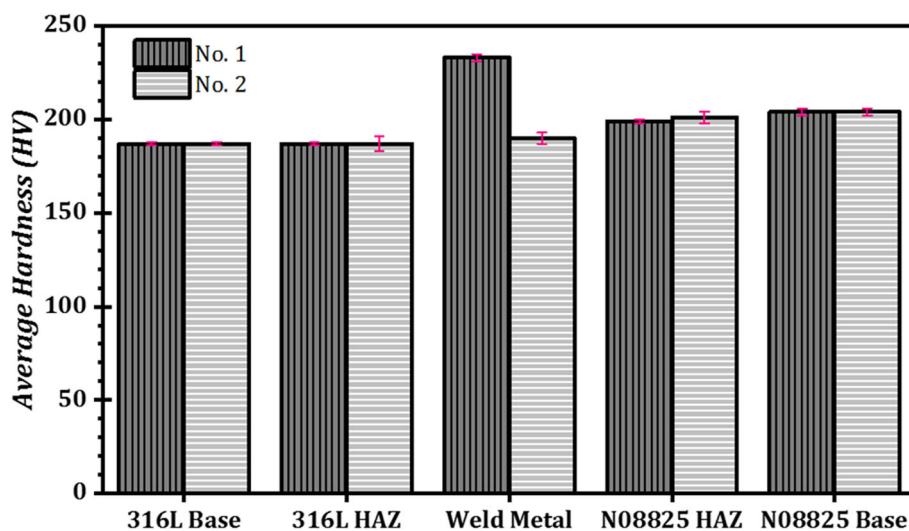

Fig. 13 Variations in the microhardness values across the No. 1 and No. 2 weldments
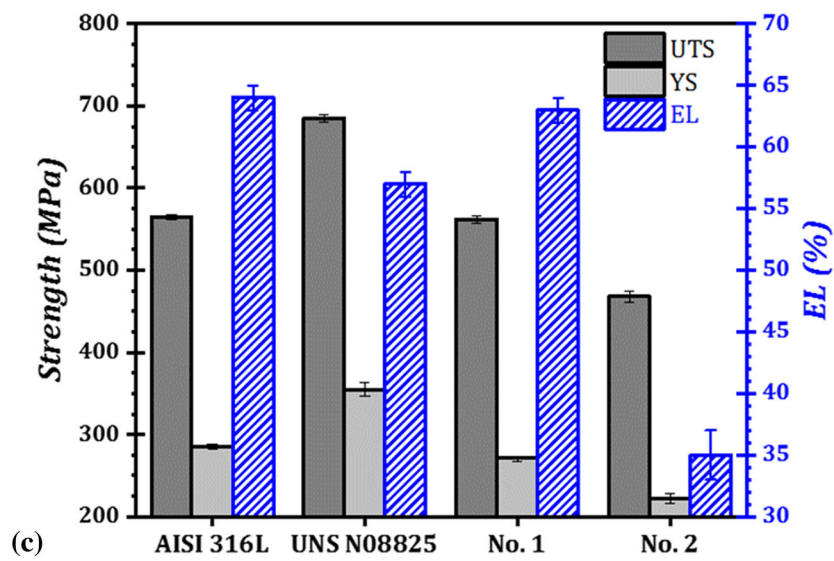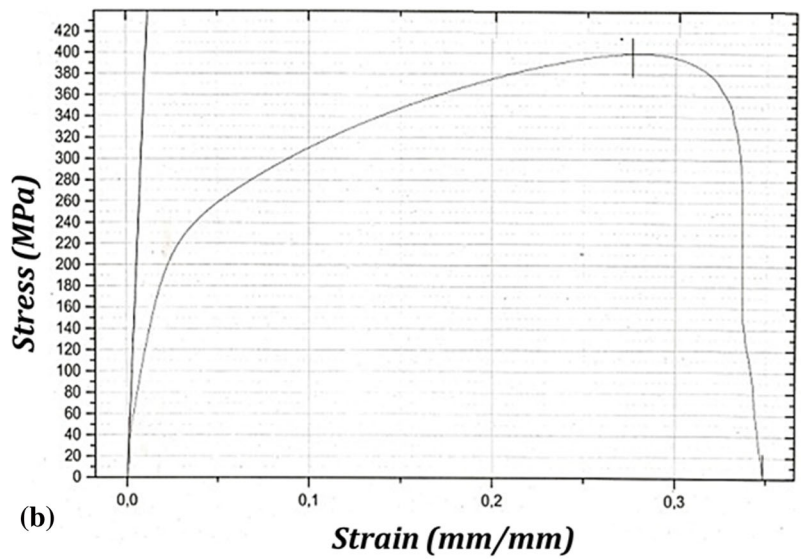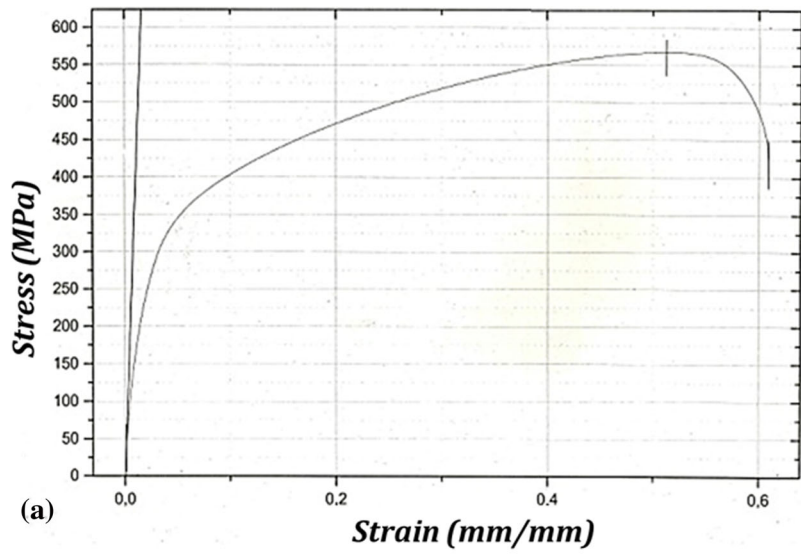
Fig. 14 The results of the tensile tests: (a) stress–strain curve of sample No. 1, (b) stress–strain curve of sample No. 2, and (c) average values of tensile properties (EL: Elongation, UTS: Ultimate Tensile Strength, YS: Yield Strength)
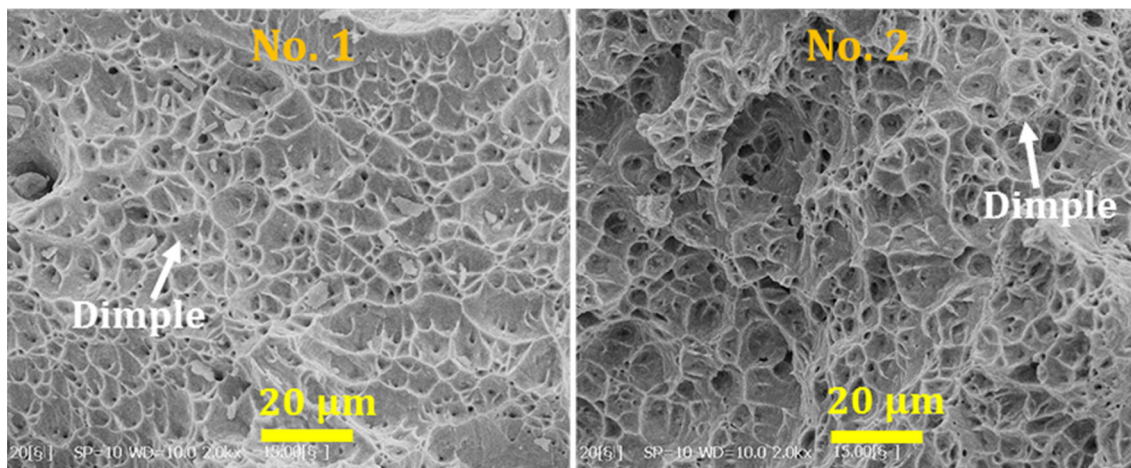
Fig. 15 Fractography of tensile specimens

highly dependent on the thermal cycles experienced by the materials during welding. The results of our previous research (Ref 12) also highlighted the effect of the thermal cycles on the microtexture of HAZs. According to the reference (Ref 12) regarding the UNS S32750 super duplex stainless steel/UNS N08825 Ni-based superalloy joints, when the same filler wire is used, changes in the welding current mode (i.e., pulsed current vs. continues current) result in significant changes in the microtexture of HAZs. The outcome of the current study indicates that the type of filler wire is another factor affecting the microtexture of the weldments.

3.3 Assessment of Mechanical Properties

The mechanical behavior of the weldments was investigated in terms of hardness and tensile tests at room temperature. Figure 13 displays the results of the microhardness tests. The obtained results indicated that No. 1 weld metal (233 HV) showed the highest hardness value. In addition, the hardness values of HAZs were similar to the related base metals. Figure 14 illustrates the results of the transverse tensile tests. As can be seen, the strength and elongation of No. 1 weldment were similar to those of the weaker base metal (i.e., AISI 316L). On the other hand, the strength of No. 2 weldments was slightly lower than the 316L base metal. Moreover, a significant reduction in elongation of No. 2 weldment was observed as compared to the 316L base metal, while the elongation of No. 1 weldment (63%) was similar to that of the 316L parent metal (65%). It is worth mentioning that the location of the tensile fracture for both No. 1 and No. 2 weldments was 316L HAZ. The obtained results were in agreement with the previous work (Ref 7), where the authors reported that the fracture location of UNS N08825/AISI 316 welds was 316 HAZs and/or weld zone. However, in the current research, the results of the hardness tests did not show a significant reduction in hardness values of 316L HAZs. In other words, the results of the hardness tests were not in good agreement with those of the tensile tests. It could be attributed to the fact that the hardness data revealed the local mechanical response of the weldments, while the data related to the tensile strength showed the global mechanical behavior of the weldments. Observations of the fracture surfaces (Fig. 15) after tensile testing indicated that both No. 1 and No. 2 weldments underwent ductile fracture mode, as a result of the formation of dimples and voids in the fracture surfaces.

Considering the chemical composition of the base metals and filler wires (Table 1), the ERNiCrMo-3 filler wire consisted of significant amounts of some elements, like 0.1% C and 8% Mo, which could provide better solid-solution strengthening effect in the weld zone, as compared to the ER308L filler wire (Ref 29, 36). Moreover, as explained in Sect. 3.1, some NbC precipitates were formed within the matrix of No. 1 weld metal. These precipitates could improve the strength of No.1 weld metal by applying pinning effect on the mobile dislocations, i.e., Orowan strengthening mechanism. Overall, it can be said that No. 1 weldment showed better hardness and higher strength than No. 2 weldment, as a result of the presence of NiC carbides, as well as solid-solution strengthening effect in the weld metal. The results were in good agreement with the previous works (Ref 37, 38), where the researchers reported that Nb- and Mo-bearing Ni-based superalloys weld metals showed better strength and hardness than the weld metals employing the austenitic stainless steels filler wires.

The results of the microhardness tests indicated that the average microhardness values of HAZs were similar to the related base metal. As explained in Sect. 3.1, abnormal grain growth took place in both UNS N08825 HAZs and 316L HAZs. Based on the well-known Hall–Petch equation, the higher the grain size, the lower the hardness (or strength) (Ref 39). Thus, it is expected that the presence of the abnormal grain growth resulted in a decrease in strength and/or hardness of HAZs. However, the results of the tensile tests (i.e., fracture location in the weldments) demonstrated that the presence of the abnormal grain growth in UNS N08825 HAZs had no negative effect on the strength of the weldments. Since the activation of the slip systems in a specific material is dependent on the orientation of grains, the strength of a material depends on the relative orientation of its grains with respect to the direction of the applied stress.

Taylor factor and Schmid factor are typically used to describe the correlation between the strength and the orientation of grains (Ref 40, 41). Because Schmid factor only considers the angles between loading directions and shear planes, it could be used to explain the stresses-orientations dependence in single crystals. On the other hand, Taylor factor could be
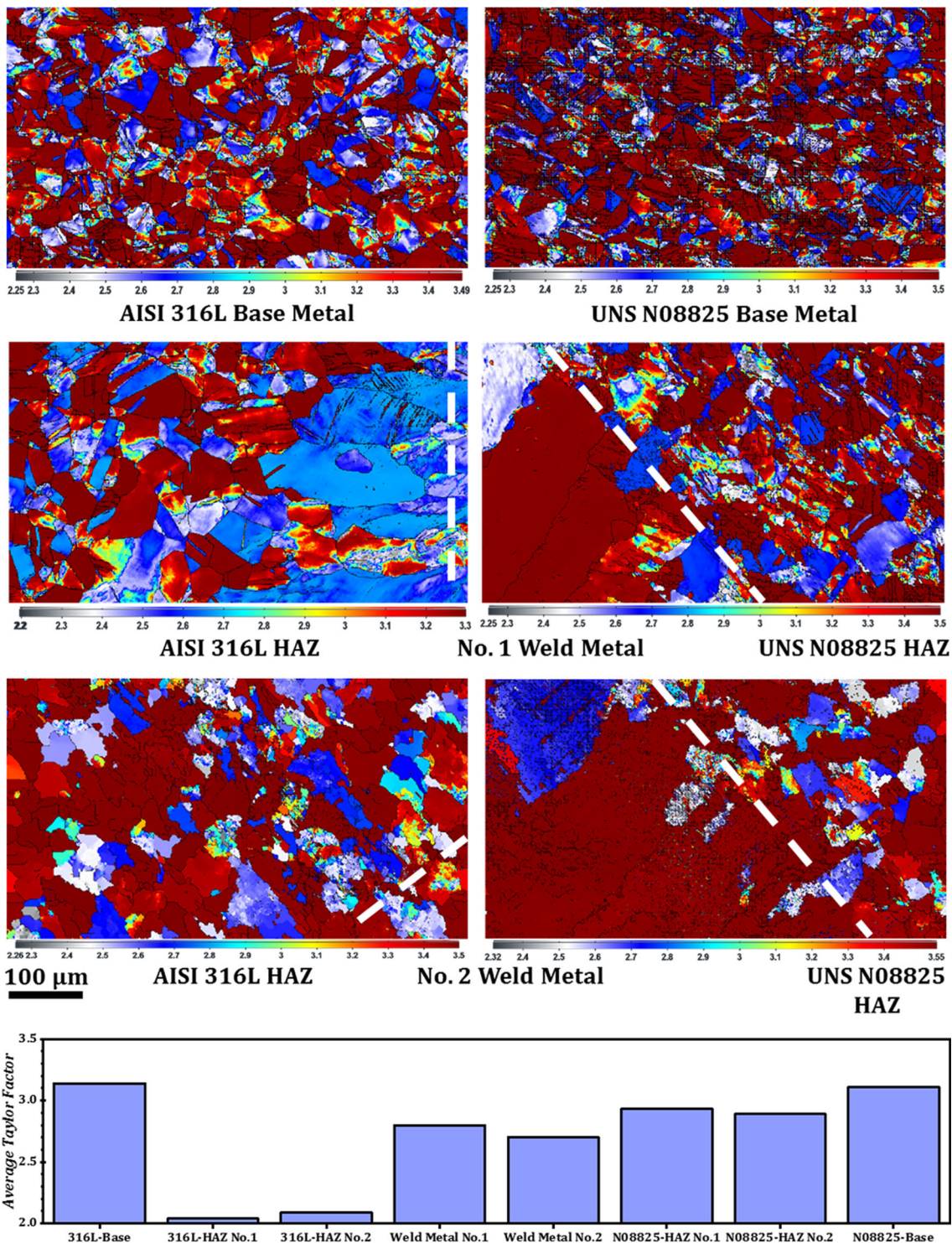
Fig. 16 Taylor factor maps of the weldments with respect to X loading direction

employed to describe the plastic deformation in textured materials with respect to the grain-to-grain effects. According to the Taylor theory, at least five slip systems should be activated in individual grains to onset of plastic deformation and accommodate the grain-to-grain incompatibilities regarding the loading direction (Ref 40, 42). Figure 16 depicts the Taylor factor maps of the weldments with respect to X loading direction. It is worth mentioning that in Fig. 16, the calculations

were based on the {111} <110> slip system, which is one of the preferred slip systems in an FCC crystal (Ref 40). It is well accepted that (Ref 42, 43) the higher the Taylor factor, the higher the flow stress. In other words, an increase in the Taylor factor in grains shows the increment of texture strengthening effect. As can be seen, the average Taylor factor values in UNS N08825 HAZs were almost similar to those in the related base metal. Thus, it can be said that texture strengthening mecha-

nism could be dominated in UNS N08825 HAZs. It could be a reason for explaining why the presence of abnormal growth in UNS N08825 HAZs did not have a negative effect on the strength of the weldments. In the weld metals, the average Taylor factor values were almost similar to those of the base metals. Hence, it can be said that the improvement in the strength resulting from the orientations of grains in the weld metals was almost similar to that in the base metals. Regarding 316L HAZs, the Taylor factor maps revealed that the average Taylor factor values of both No. 2 and No. 1 samples were lower than those of the base metals. In addition, 316L HAZ of both No. 1 and No. 2 samples underwent abnormal grain growth. Hence, deterioration of strength in 316L HAZs could result from the texture effect, as well as the occurrence of grain growth. Overall, these pieces of evidence elucidate the reason the fracture location for the weldments was 316L HAZs.

4. Conclusions

i. A significant decrease in the fractions of low ΣCSL boundaries was observed in 316L HAZs as compared to 316L base metal, while it was indicated that higher fractions of low ΣCSL boundaries were formed in UNS N08825 HAZs as compared to the related base metal.

ii. Evaluations of microtexture variations in the weldments showed that the initial texture components formed in the base metals were replaced by new ones in HAZs. In addition, the orientation of grain within the weld zones was found to be random.

iii. It was demonstrated that at the same HI value, changes in the type of the used filler wire had a significant effect on the texture components formed within HAZs.

iv. In good agreement with the existing literature works, abnormal grain growth was observed in HAZs. Regarding UNS N08825 side, grain growth had no significant effect on the strength of HAZs as a result of the activation of texture strengthening mechanism. However, 316L HAZs were the weakest part of the weldments because the texture strengthening mechanism was not dominated.

v. The weldment employing the ERNiCrMo-3 filler wire showed better tensile behavior than that employing ER308L filler wire. Hence, based on the obtained results, ERNiCrMo-3 filler wire was recommended to perform the dissimilar welding between UNS N08825 and AISI 316L alloys.

Conflict of interest

The authors declare that they have no known competing financial interests or personal relationships that could have appeared to influence the work reported in this paper.

Ethical standards

The article was conducted according to ethical standards. This manuscript has been prepared by the contribution of all authors, it is the original author's work, it has been solely submitted to this journal, and if accepted, it will not be submitted to other journals.

References

1. K.D. Ramkumar, P.S. Goutham, V.R. Krishna, A. Chandrasekhar, S. Dev, W. Sunny, S. Prabhakaran, S. Kalainathan and R. Sridhar, Influence of Laser Peening on the Tensile Strength and Impact Toughness of Dissimilar Welds of Inconel 625 and UNS S32205, *Mater. Sci. Eng. A.*, 2016, **676**, p 88–99. https://doi.org/10.1016/j.msea.2016.08.104

2. S. Meco, S. Ganguly and S. Williams, Effect of Laser Processing Parameters on the Formation of Intermetallic Compounds in Fe-Al Dissimilar Welding, *J. Mater. Eng. Perform.*, 2014, **23**, p 3361–3370. https://doi.org/10.1007/s11665-014-1106-5

3. S. Sharma, R.V. Taiwade and H. Vashishtha, Effect of Continuous and Pulsed Current Gas Tungsten Arc Welding on Dissimilar Weldments Between Hastelloy C-276/AISI 321 Austenitic Stainless Steel, *J. Mater. Eng. Perform.*, 2017, **26**, p 1146–1157. https://doi.org/10.1007/s11665-017-2570-5

4. S. Zhou, G. Ma, D. Chai, F. Niu, J. Dong and D. Wu, Nickel-Based Alloy/Austenitic Stainless Steel Dissimilar Weld Properties Prediction on Asymmetric Distribution of Laser Energy, *Opt. Laser Technol.*, 2016, **81**, p 33–39. https://doi.org/10.1016/j.optlastec.2016.01.017

5. M.A. Derakhshi, J. Kangazian and M. Shamanian, Electron Beam Welding of Inconel 617 to AISI 310: Corrosion Behavior of Weld Metal, *Vacuum*, 2019, **161**, p 371–374. https://doi.org/10.1016/j.vacuum.2019.01.005

6. M. Tümer, T. Mert and T. Karahan, Investigation of Microstructure, Mechanical, and Corrosion Behavior of Nickel-Based Alloy 625/Duplex Stainless Steel UNS S32205 Dissimilar Weldments using ERNiCrMo-3 Filler Metal, *Weld World*, 2020 https://doi.org/10.1007/s40194-020-01011-0

7. M. Safari, H. Mostaan and E. Derakhshan, Microstructual and Mechanical Studies of the Dissimilar Tabular Joints of Incoloy Alloy 825 and AISI 316 Stainless Steel, *J. Marine Eng. Technol.*, 2018 https://doi.org/10.1080/20464177.2018.15088055

8. T. Ramkumar, M. Selvakumar, P. Narayanasamy, A.A. Begam, P. Mathavan and A.A. Raj, Studies on the Structural Property, Mechanical Relationships and Corrosion Behaviour of Inconel 718 and SS 316L Dissimilar Joints by TIG Welding Without using Activated Flux, *J. Manuf. Process.*, 2017, **30**, p 290–298. https://doi.org/10.1016/j.jmapro.2017.09.028

9. G. Chandrasekar, C. Kailasanathan and M. Vasundara, Investigation on Un-Peened and Laser Shock Peened Dissimilar Weldments of Inconel 600 and AISI 316L Fabricated using Activated-TIG Welding Technique, *J. Manuf. Process.*, 2018, **35**, p 466–478. https://doi.org/10.1016/j.jmapro.2018.09.004

10. H. Ramakrishnan, G. Sakthi, V. Santhosh, M. Ravichandran, Mechanical, Microstructural Evaluation and Optimisation of Laser Welded AISI 316l and Incoloy 825 (UNS SO8825) Alloy, *AIP Conference Proceedings*. Vol. 2283. No. 1. AIP Publishing LLC (2020)

11. A. Kulkarni, D.K. Dwivedi and M. Vasudevan, Microstructure and Mechanical Properties of A-TIG Welded AISI 316L SS-Alloy 800 Dissimilar Metal Joint, *Mater. Sci. Eng. A.*, 2020, **790**, p 139685. https://doi.org/10.1016/j.msea.2020.139685

12. J. Kangazian and M. Shamanian, Micro-Texture and Corrosion Behavior of Dissimilar Joints of UNS S32750 Stainless Steel/UNS N08825 Ni-Based Superalloy, *Mater. Charact.*, 2019, **155**, p 109802. https://doi.org/10.1016/j.matchar.2019.109802

13. Beausir J-JFB. Analysis tools for Electron and X-Ray diffraction; 2017. ATEX-Software; 2017. www.atex-software.eu

14. J.C. Lippold and D.J. Kotecki, *Welding Metallurgy and Weldability of Stainless Steels*, Wiley, Hoboken, 2005

15. Q. Bai, Q. Zhao, S. Xia, B. Wang, B. Zhou and C. Su, Evolution of Grain Boundary Character Distributions in Alloy 825 Tubes during High Temperature Annealing: Is Grain Boundary Engineering Achieved through Recrystallization or Grain Growth?, *Mater. Charact.*, 2017, **123**, p 178–188. https://doi.org/10.1016/j.matchar.2016.11.016

16. S. Goel, H. Mehtani, S. Yao, I. Samajdar, U.T.A. Klement and S. Joshi, As-Built and Post-treated Microstructures of an Electron Beam Melting (EBM) Produced Nickel-Based Superalloy, *Metall. Mater. Trans. A.*, 2020 https://doi.org/10.1007/s11661-020-06037-z

17. S. Tokita, H. Kokawa, Y.S. Sato and H.T. Fujii, In situ EBSD Observation of Grain Boundary Character Distribution Evolution during Thermomechanical Process Used for Grain Boundary Engi-

neering of 304 Austenitic Stainless Steel, *Mater. Charact.*, 2017, **131**, p 31–38. https://doi.org/10.1016/j.matchar.2017.06.032

18. G. Sayiram and N. Arivazhagan, Microstructural Characterization of Dissimilar Welds Between Incoloy 800H and 321 Austenitic Stainless Steel, *Mater. Charact.*, 2015, **102**, p 180–188. https://doi.org/10.1016/j.matchar.2015.03.006

19. J.D. Busch, J.J. Debarbadillo and M.J.M. Krane, Flux Entrapment and Titanium Nitride Defects in Electroslag Remelting of Incoloy Alloys 800 and 825, *Metall. Mater. Trans. A.*, 2013, **44**, p 5295–5303. https://doi.org/10.1007/s11661-013-1659-1

20. M. Sireesha, V. Shankar, S.K. Albert and S. Sundaresan, Microstructural Features of Dissimilar Welds Between 316LN Austenitic Stainless Steel and Alloy 800, *Mater. Sci. Eng. A.*, 2000, **292**, p 74–82

21. C. Hu, S. Xia, H. Li, T. Liu, B. Zhou, W. Chen and N. Wang, Improving the Intergranular Corrosion Resistance of 304 Stainless Steel by Grain Boundary Network Control, *Corros. Sci.*, 2011, **53**, p 1880–1886. https://doi.org/10.1016/j.corsci.2011.02.005

22. S. Emami and T. Saeid, A Comparative Study on the Microstructure Development of Friction Stir Welded 304 Austenitic, 430 Ferritic, and 2205 Duplex Stainless Steels, *Mater. Chem. Phys.*, 2019, **237**, p 121833. https://doi.org/10.1016/j.matchemphys.2019.121833

23. H. Ming, Z. Zhang, J. Wang, E. Han, P. Wang and Z. Sun, Microstructure of a Safe-End Dissimilar Metal Weld Joint (SA508-52-316L) Prepared by Narrow-Gap GTAW, *Mater. Charact.*, 2017, **123**, p 233–243. https://doi.org/10.1016/j.matchar.2016.11.029

24. J.C. Lippold, *Welding Matellurgy and Weldbility*, Wiley, Hoboken, 2015

25. R.S. Razavi, Laser Beam Welding of Waspaloy: Characterization and Corrosion Behavior Evaluation, *Optic Laser Technol.*, 2016, **82**, p 113–120. https://doi.org/10.1016/j.optlastec.2016.03.011

26. D. Jadhav, S. Dadbakhsh, L. Goossens, J. Kruth, J. Van Humbeeck and K. Vanmeensel, Influence of Selective Laser Melting Process Parameters on Texture Evolution in Pure Copper, *J. Mater. Process. Technol.*, 2019, **270**, p 47–58. https://doi.org/10.1016/j.jmatprotec.2019.02.022

27. J.N. DuPont, J.C. Lippold and S.D. Kiser, *Welding Metallurgy and Weldability of Nickel Base Alloys*, Wiley, Hoboken, 2009

28. K.D. Ramkumar, A. Chandrasekhar and A. Kumar, Effect of Filler Metals on the Structure—Property Relationships of Continuous and Pulsed Current GTA Welds of AISI 430 and AISI 904L, *Metallogr. Microstruct. Anal.*, 2015, **4**, p 525–541. https://doi.org/10.1007/s13632-015-0236-y

29. K.D. Ramkumar, A. Singh, S. Raghuvanshi, A. Bajpai, T. Solanki, M. Arivarasu, N. Arivazhagan and S. Narayanan, Metallurgical and Mechanical Characterization of Dissimilar Welds of Austenitic Stainless Steel and Super-Duplex Stainless Steel—A Comparative Study, *J. Manuf. Process.*, 2015, **19**, p 212–232. https://doi.org/10.1016/j.jmapro.2015.04.005

30. R.S.K. Devendranath and R.N. Arivazhagan, Characterization of Microstructure, Strength , and Toughness of Dissimilar Weldments of Inconel 625 and Duplex Stainless Steel SAF 2205, *Acta Metall. Sinica (Engl. Lett.)*, 2014, **27**, p 1018–1030. https://doi.org/10.1007/s40195-014-0116-5

31. C.C. Silva, H. Cordeiro, D. Miranda, M. Ferreira, J. Pereira, C. Ramos, M. Afonso and A. Jose, Original Article New Insight on the Solidification Path of an Alloy 625 Weld Overlay, *Integr. Med. Res.*, 2013, **2**, p 228–237. https://doi.org/10.1016/j.jmrt.2013.02.008

32. A. Moteshakker, I. Danaee, S. Moeinifar and A. Ashrafi, Hardness and Tensile Properties of Dissimilar Welds Joints Between SAF 2205 and

AISI 316L, *Sci. Technol. Weld. Join.*, 2015, **21**, p 1–10. https://doi.org/10.1179/1362171815Y.0000000062

33. J. Verma and R.V. Taiwade, Effect of Welding Processes and Conditions on the Microstructure, Mechanical Properties and Corrosion Resistance of Duplex Stainless Steel Weldments—A Review, *J. Manuf. Process.*, 2017, **25**, p 134–152. https://doi.org/10.1016/j.jmapro.2016.11.003

34. A. Eghlimi, M. Shamanian, M. Eskandarian, A. Zabolian and J.A. Szpunar, Characterization of Microstructure and Texture Across Dissimilar Super Duplex/Austenitic Stainless Steel Weldment Joint by Super Duplex Filler Metal, *Mater. Charact.*, 2015, **106**, p 27–35. https://doi.org/10.1016/j.matchar.2015.05.017

35. F.J. Humphreys and M. Hatherly, *Recrystallization and Related Annealing Phenomena*, Elsevier, Amsterdam, 2012

36. K.D. Ramkumar, A. Harendra, A. Anil, M. Atharva, C. Vishnu, D. Arun, M.G. Vijay, W. Sunny, A. Chatterjee, J. Abraham and J. Abraham, Microstructure, Mechanical Properties and Biocorrosion Behavior of Dissimilar Welds of AISI 904L and UNS S32750, *J. Manuf. Process.*, 2017, **30**, p 27–40. https://doi.org/10.1016/j.jmapro.2017.09.001

37. H. Shah Hosseini, M. Shamanian and A. Kermanpur, Characterization of Microstructures and Mechanical Properties of Inconel 617/310 Stainless Steel Dissimilar Welds, *Mater. Charact.*, 2011, **62**, p 425–431. https://doi.org/10.1016/j.matchar.2011.02.003

38. A.H. Saedi, E. Hajjari and S.M. Sadrossadat, Microstructural Characterization and Mechanical Properties of TIG-Welded API 5L X60 HSLA Steel and AISI 310S Stainless Steel Dissimilar Joints, *Metall. Mater. Trans. A.*, 2018, **49**(11), p 5497–5508. https://doi.org/10.1007/s11661-018-4890-y

39. H.B. Li, Z.H. Jiang, H. Feng, S.C. Zhang, L. Li, P.D. Han, R.D.K. Misra and J.Z. Li, Microstructure, Mechanical and Corrosion Properties of Friction Stir Welded High Nitrogen Nickel-Free Austenitic Stainless Steel, *Mater. Des.*, 2015, **84**, p 291–299. https://doi.org/10.1016/j.matdes.2015.06.103

40. A. Keshavarzkermani, R. Esmaeilizadeh, U. Ali, P.D. Enrique, Y. Mahmoodkhani, N.Y. Zhou, A. Bonakdar and E. Toyserkani, Controlling Mechanical Properties of Additively Manufactured Hastelloy X by Altering Solidification Pattern during Laser Powder-Bed Fusion, *Mater. Sci. Eng. A.*, 2019, **762**, p 138081. https://doi.org/10.1016/j.msea.2019.138081

41. J. Myoung, J. Min, J. Yu, J. Gi, Y. Seong, S. Hong and H. Seop, Effects of Microstructure and Internal Defects on Mechanical Anisotropy and Asymmetry of Selective Laser-Melted 316L Austenitic Stainless Steel, *Mater. Sci. Eng. A.*, 2019, **763**, p 138152

42. J. Min, J. Choe, H. Keun, S. Son, J. Jung, T. Kim, J. Yu, J. Gi and H. Seop, Synergetic Strengthening of Additively Manufactured (CoCr-FeMnNi) 99 C 1 High-Entropy Alloy by Heterogeneous Anisotropic Microstructure, *Addit. Manuf.*, 2020, **35**, p 101333. https://doi.org/10.1016/j.addma.2020.101333

43. S.Y. Liu, H.Q. Li, C.X. Qin, R. Zong and X.Y. Fang, The Effect of Energy Density on Texture and Mechanical Anisotropy in Selective Laser Melted Inconel 718, *Mater. Des.*, 2020, **191**, p 108642. https://doi.org/10.1016/j.matdes.2020.108642